# Investigation of Transport Properties and Dielectric Studies in $La_{(0.9)}Bi_{(0.1)}MnO_3$ Manganite

V. Punith Kumar*

*Department of Physics, B. M. S. College of Engineering, Bengaluru, Karnataka 560019, India*

Received: 06.11.2024 & Accepted: 10.30.2025

Doi: 10.12693/APhysPolA.147.383 *e-mail: pkv.science@gmail.com

Low bismuth doping in lanthanum manganite is studied in detail for its unusual electrical conductivity and dielectric properties. The direct current electrical conductivity measurements exhibit proper semiconducting (or insulating) nature without any phase transitions. The low temperature direct current electrical conduction is due to the Mott-variable range hopping mechanism in the absence of the magnetic field ($H = 0$ T). However, in the presence of magnetic field ($H = 8$ T) the direct current electrical conduction switches to the Shklovskii–Efros-variable range hopping mechanism. The high-temperature direct current electrical conduction is governed by the Greaves-variable range hopping mechanism both at $H = 0$ T and 8 T. The dielectric properties studied as a function of temperature and frequency exhibit a multiple relaxation process, which can be attributed due to the Debye + Maxwell–Wagner relaxation mechanisms. The frequency-dependent alternating current conductivity studied under constant temperatures further correlates with polaronic hopping transport mechanisms, as observed in direct current electrical conductivity measurements.

topics: direct current (DC) and alternating current (AC) conductivity, polaronic transport, variable range hopping, dielectric constant

## 1. Introduction

The perovskite oxide materials that correlate with properties such as magnetism and ferroelectricity have gained significant interests from long time due to their exceptional device applications and intriguing underlying physics [1]. One such oxide material is $BiMnO_3$, which is studied extensively for its simultaneous exhibition of ferromagnetic and ferroelectric properties [2]. The ferromagnetic properties are understood to be originating from the double exchange (DE) or super-exchange (SE) interactions between the nearest neighboring Mn cations via oxygen forming as a bridge associated due to the specific $d_z^2$ orbital ordering in $Mn^{3+}$ (or $Mn^{4+}$). Whereas the ferroelectric property arises due to the highly polarized and isolated $6s^2$ lone pair electron of $Bi^{3+}$ ions, which induces significant structural distortions [3]. Compared to $BiMnO_3$, the $d_z^2$ orbital in $LaMnO_3$ undergoes anti-ferro distortive charge ordering and results in orthorhombic ($O'$) or rhombohedral ($R\bar{3}c$) crystal structure [3, 4]. Previous studies of $LaMnO_3$, explained in [5], showed that if the percentage of $Mn^{4+}$ exceeds a significant amount ($> 20\%$), the room temperature structure becomes rhombohedral. In the context of lanthanum bismuth-based perovskite manganite oxides, the relationship between the structural ordering and the influences of magneto-transport properties have gained considerable interests [6]. Potential manganite perovskites, which show simultaneous ferromagnetic and insulating properties, are considered as a significant material for spintronics technology [7]. The recent surge of interest in these types of materials is also due to the necessity of using electronic microdevices, which is why the focus has been on the production of read heads in spintronic components for data recording and reliable data storage components that can operate at room temperatures and under extreme conditions [7]. In such materials, the correlation between the electrical charge and spins of the electrons are used to bring about spin-dependent electronic functional property, such as colossal magnetoconductive phenomenon. The highly-insulating states around the critical temperature $T_C$ in some manganites are very responsive to the applied magnetic field, which influences the transport properties and provides the means to understand the mechanism such as magnetoconductivity [8]. The creation of tetravalent manganese ions ($Mn^{4+}$) when substituted with divalent/trivalent cations results in the improvement of the transport property via DE or SE. Many researchers [8–10] tried to explain the influence of the magnetic field on the electrical transport phenomenon based on the electron band transport mechanism for most compounds.

In the present case, however, this mechanism may not apply suitably because of the insulating behavior of some manganites around $T_C$. Due to these factors, compound comprisin both lanthanum and bismuth-based manganites are interesting to study their physical properties and understand the role of different mechanisms responsible for the electrical transport. The $La_{0.9}Bi_{0.1}MnO_3$ compound synthesized from $LaMnO_3$ by the necessary substitution for trivalent La ions with trivalent Bi ions belongs to the separate group of manganites, which exhibits robust physical properties. Unlike divalent substitution at La site, these manganites are useful for their practical purposes in device fabrications and advanced technological applications in storage and sensors [11].

## 2. Experimental setup

The studied sample $La_{0.9}Bi_{0.1}MnO_3$ is synthesized using a conventional solid-state reaction method [12, 13]. The basic ingredients of $La_2O_3$, $Bi_2O_3$ and $MnO_2$ are procured from SIGMA ALDRICH & Co. with a purity of 99.9% each. Following the individual ingredients of $La_2O_3$ (preheated around 900°C to remove moistures and impurities), $Bi_2O_3$, and $MnO_2$ were stoichiometrically weighed and mixed in an agate mortar in the presence of acetone to get compositional mixtures. The greyish sample mixture was then fired in furnace at 600°C, followed by sintering at 750°C with intermittent grindings. The greyish powdered sample turned dark grey and was pelletized using a 13 mm die at an applied pressure of 98 kilo-Pa and sintered at 850°C for 45 h with slow heating cycles due to the volatility of Bi. This step was repeated twice in order to get a perfect pellet without any breaks and internal cracks. To verify the phase purity of the sintered sample, X-ray diffraction measurement was carried out using a Cu $K_\alpha$ radiation source. The sample crystalizes into a rhombohedral perovskite's crystal symmetry belonging to the $R\bar{3}c$ space group with lattice parameters $a = 5.529$ Å, $b = 5.529$ Å and $c = 13.378$ Å — further, the cell volume is calculated to be $V = 409.06$ (Å)$^3$. To verify the morphology and composition of the sample, a scanning electron microscopic (SEM) imaging technique was employed, equipped with an energy dispersive X-ray spectroscopic (EDS) measurement system. From the SEM image, the grain shapes are found to be spherically symmetric with no significant porosity as reported in [13]. Direct current (DC) electrical conductivity measurement both as a function of temperature and magnetic field were carried out using an Oxford Spectromag 10 T superconducting magnet with the standard four probe contact method. Frequency-dependent complex dielectric measurements at constant temperatures were carried out using a Novo-control alpha impedance analyzer RMS

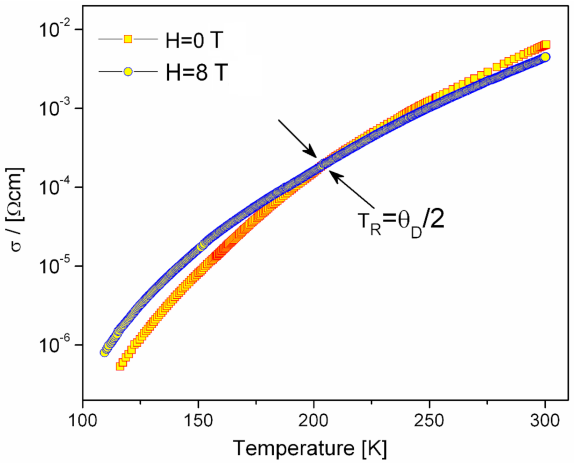


Fig. 1. DC electrical conductivity measurements for the sample studied at the magnetic fields $H = 0$ T and 8 T are shown on a $y$-logarithmic scale.

AC voltage of 1 V (AC — alternating currect). The sample in the pellet form was sandwiched between the electrodes of a Novo-control BDS 1200 sample cell.

## 3. Results and discussions

In Fig. 1, the smooth variation of the DC electrical conductivity ($\sigma$) vs temperature ($T$) measured at the constant applied magnetic field values $H = 0$ T and 8 T is shown, from room temperature ($T = 300$ K) up to low temperature ($T = 100$ K). Below $T = 100$ K the conductivity measurements exceeded the instrumental limit ($(\times 10^{-6})$ [$(\Omega\,\mathrm{cm})^{-1}$]) and started to show random fluctuations. It can be observed that the sample shows an insulating (semiconducting) nature throughout the measured temperature range without any specific phase transition. From this nature, it follows that low concentration of $Bi^{3+}$ substitution slightly disrupts the Mn–O octahedra and hamper cooperative Jahn–Teller (JT) distortions [14].

The influence of constant applied magnetic field ($H = 8$ T) improves $\sigma$ compared to the original data without the application of magnetic field ($H = 0$ T). But at temperature $T = 204$ K, hereafter referred as reversing temperature ($T_R = \theta_D/2$) the $\sigma$ values measured at $H = 8$ T show crossover effect and the values of $\sigma$ decreases well below the values of $\sigma$ measured at $H = 0$ T. This behaviour is distinctively observed for polaronic (small or large) hopping conduction and depends on thermally activated energies. Further it can be understood as the temperature increases the $Bi^{3+}$ ions in the sample starts to hamper the conduction process through

TABLE I

The computed and fitted values obtained from various experimental models have been enlisted for $La_{0.9}Bi_{0.1}MnO_3$.

| $H$ [T] | Temp. | $E_A$ [eV] | SPHC model $E_D$ [eV] | $J/\varphi$ | $\gamma_p$ | Critical exponent $\nu$ | $R_h$ [nm] | $E_h \times 10^{-3}$ [eV] | Mott's model $N(E_{F_M}) \times 10^{24}$ [$eV^{-1}m^{-3}$] | Greaves model $N(E_{F_G}) \times 10^{24}$ [$eV^{-1}m^{-3}$] |
|---|---|---|---|---|---|---|---|---|---|---|
| 0 | $T < T_R$ | 0.125 | 0.135 | 0.173 | 15.306 | 0.961 | – | – | 0.46 | – |
| | $T > T_R$ | 0.207 | 0.216 | 0.108 | 24.490 | 1.115 | 0.322 | 6.182 | – | 0.42 |
| 8 | $T < T_R$ | 0.106 | 0.119 | 0.196 | 13.531 | 0.883 | – | – | 0.89 | – |
| | $T > T_R$ | 0.184 | 0.196 | 0.119 | 22.222 | 1.074 | 0.307 | 6.119 | – | 0.86 |

significant vibrations and distortion of the Mn cationic polaron pathways. This eventually decreases electrical conductivity even in the presence of $H = 8$ T due to the random distributions of the available neighbouring sites and significant thermal fluctuations. Hirashima et al. [15] expressed '$\theta_D$' as the Debye temperature designated for the vibrational energy spectrum of a polycrystalline sample, defined as

$$h\nu_0 = k_B\theta_D = \frac{h\nu}{2\pi}\left(\frac{6\pi^2 N}{V}\right)^{\frac{1}{3}}, \quad (1)$$

where $h$ is Planck's constant, $\nu_0$ is the optical phonon frequency, $N$ is the number of atoms per unit cell, $V$ is the volume and $k_B$ is the Boltzmann's constant. Also, the polaronic transport in the studied compound depend upto a certain level of specific phonon vibrational energy ($\nu_0$) and which is also optically active falling in the range of $10^{12}$–$10^{14}$ $s^{-1}$. The calculated value of $\nu_0$ from the above relation is found to be $4.26 \times 10^{12}$ $s^{-1}$, which further satisfy the above criteria. This type of feature is unique in such kind of $Bi^{3+}$ doped $LaMnO_3$ manganites, where previously not been fully explored and can be distinctively observed for the polaronic type of conduction which depends on the temperature dependent activation energies [16].

To calculate the activation energies required for this type of polaronic transport, the thermally activated conduction (TAC) model has been studied, which can be expressed as

$$\sigma(T) = \sigma_0 \exp\left(\frac{-E_A}{k_B T}\right), \quad (2)$$

where $E_A$ is the activation energy, and the pre-exponential factor $\sigma_0$ can be expressed as

$$\sigma_0 = \frac{f_0 N_D e^2 R_p^2}{k_B}\left(S(1-S)\right)\exp\left(-2\alpha R_p\right), \quad (3)$$

where $f_0$ is the longitudinal optical frequency, $R_p$ is the distance between nearest neighbouring sites, $\alpha$ is the inverse localization length used for localized states at $Mn^{3+}/Mn^{4+}$ cations, $S$ is the fraction of available sites occupied by the polaron, and $N_D$ is the $Mn^{3+}/Mn^{4+}$ ion density [17]. In Fig. 2, the TAC data were plotted on a logarithmic scale and linearly fitted in separate, distinct regions where the slopes get changed both at $H = 0$ T and 8 T for lower

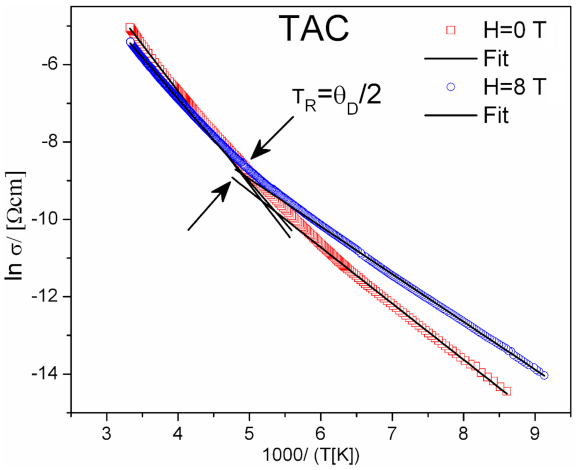


Fig. 2. The plot of $\ln(\sigma/[\Omega\ \mathrm{cm}])$ vs $1000/T$ $[K^{-1}]$ for the studied sample at the magnetic field $H = 0$ T and 8 T is shown. The solid lines are the thermally activated conduction model fits.

temperature ($T < T_R = \theta_D/2$) and higher temperature ($T > T_R = \theta_D/2$) regions to extract the $E_A$ values, as shown in Table I. From the obtained values of $E_A$ it can be ascertained that the conduction of polaronic charge carriers between $Mn^{3+}$ and $Mn^{4+}$ is due to thermally activated hopping phenomena over the energy barriers [17]. This also indicates that the tunnelling of the charge carriers over the nearest neighbouring sites is not favoured and is usually forbidden. Further Schnakenberg et al. [18] gave a theoretical description of the adiabatic small polaronic hopping model, where the polaron disordered energy $E_D \neq 0$.

The acoustical single-phonon-assisted hopping process is attributed for electrical conduction at lower temperatures ($T < T_R = \theta_D/2$), and the optical multi-phonon-assisted hopping phenomena is attributed for electrical conduction at higher temperatures ($T > T_R = \theta_D/2$). The Schnakenberg adiabatic small polaronic hopping model describes the temperature-dependent DC electrical conductivity given by the relation

$$\sigma T = \sigma_0 \exp\left(\frac{-E_D}{k_B T}\right). \quad (4)$$

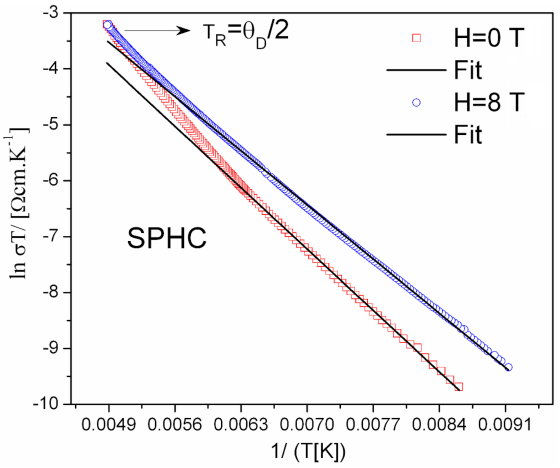


Fig. 3. The plot of $\ln(\sigma T/[\Omega\ \mathrm{cm/K}])$ vs $1/T$ $[\mathrm{K}^{-1}]$ for the sample studied at $H = 0$ T and 8 T is shown for $T < T_R = \theta_D/2$. The solid lines are the model fits.

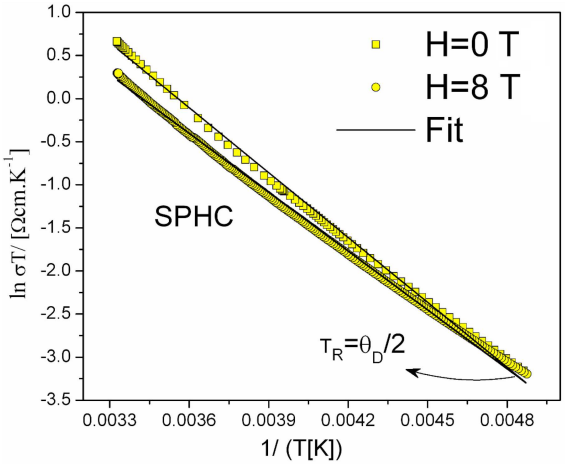


Fig. 4. The plot of $\ln(\sigma T/[\Omega\ \mathrm{cm\ K}^{-1}])$ vs $1/T$ $[\mathrm{K}^{-1}]$ for the sample studied at the magnetic field $H = 0$ T and 8 T is shown for $T > T_R = \theta_\mathrm{D}/2$. The solid lines are the model fits.

Here,

$$\sigma_0 = \sqrt{\sinh\left(\frac{h\nu_0}{k_\mathrm{B}T}\right)}\exp\left[\left(\frac{-4E_{loc}}{h\nu_0}\right)\tanh\left(\frac{h\nu_0}{4k_\mathrm{B}T}\right)\right] \tag{5}$$

with $E_{loc}$ being the localized polaronic hopping energy, and $E_D$ — the disorder in the hopping energy arising from the energy gradient between two nearest neighbouring sites due to the lattice distortions or weakening of DE. The best fits to the plot of $\ln(\sigma T/[\Omega\ \mathrm{cm\ K}^{-1}])$ vs $1/T$ $[\mathrm{K}^{-1}]$ for the sample studied at both magnetic fields $H = 0$ T and 8 T are shown in Fig. 3 for $T < T_R = \theta_\mathrm{D}/2$ and in Fig. 4 for $T > T_R = \theta_\mathrm{D}/2$.

Also, it can be observed that the Schnakenberg adiabatic small polaronic hopping model does not fit the entire range in both temperature regimes

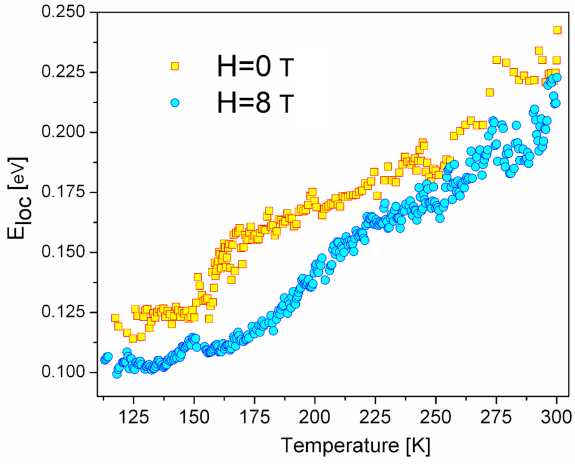


Fig. 5. The local polaronic hopping energy ($E_{loc}$) versus temperature $T$ at an applied magnetic field of 0 T and 8 T for the studied sample is shown.

described above at the applied magnetic fields $H = 0$ T and 8 T. This can be attributed to the temperature-dependent strong electron–phonon coupling, which influences the polaronic hopping over a wide range of polaronic band width between the nearest neighbouring sites [19]. Also, the Schnakenberg qualitative equation predicts a temperature-dependent localized polaronic hopping energy ($E_{loc}$), which increases with an increase in the temperature and attains random fluctuations at higher temperatures, as shown in Fig. 5. In order to identify these inequalities of polaronic hopping phenomena between the polaronic band width ($J$) and critical energy bandwidth ($\varphi$), the well-known Holstein model [20] has been adopted.

The Holstein's relation for inequalities between $J$ and $\varphi$ is given as

$$\frac{J}{\varphi} = 1.33\,\frac{k_B\theta_\mathrm{D}}{E_D}. \tag{6}$$

If the ratio $J/\varphi < 1$, then it indicates that the hopping mechanism is non-adiabatic type; and if $J/\varphi > 1$, the polaronic hopping conduction between the nearest neighbouring sites is adiabatic. From the obtained values of $J/\varphi$, shown in Table I, it is clear that the values of $J/\varphi$ are less than one $(J/\varphi < 1)$ but very close to zero — this means that the Schnakenberg adiabatic small polaronic hopping model is not sufficient to explain the polaronic hopping conduction, while simultaneously ruling out the non-adiabatic small polaronic hopping transport. Also, more clarity on this type of observation can be gained from another method, in which polaronic conduction other than the Schnakenberg adiabatic small polaronic hopping model can be determined by estimating the dimensionless small polaron coupling constant ($\gamma_p$). The parameter $\gamma_p$ is a measure of electron–phonon coupling given as $\gamma_p = 2E_D/(h\nu_0)$ and the tabulated values are listed

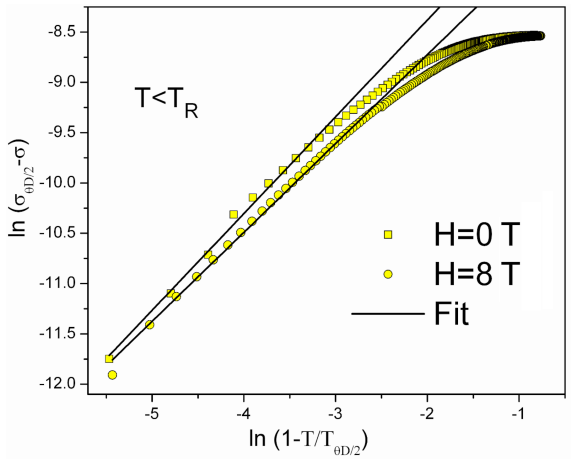


Fig. 6. Critical analysis of the electrical conductivity data for $T < T_R$ is shown. Solid lines are the model fits.

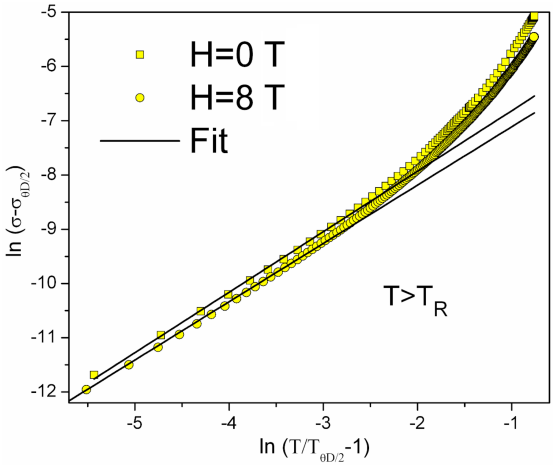


Fig. 7. Critical analysis of the electrical conductivity data for $T > T_R$ is shown. Solid lines are the model fits.

in Table I. When the obtained values of $\gamma_p$ lies in between 13 to 11, it indicates a very strong electron–phonon coupling [21] and ensures the formation of small polarons, which hop differently from the type described by Schnakenberg's adiabatic small polaronic hopping model. But the values of $\gamma_p$ does not fall in the above phenomenal limit and are very unphysical, thus indicating different type of polaronic hopping model must be responsible for the electrical conduction process. Furthermore, the ratio of polaronic mass ($m_p$) to the rigid lattice effective mass ($m^*$) have been tabulated, using the relation given by the generic relation

$$m_p = \frac{h^2}{8\pi^2 JR^2} \exp(\gamma_p) = m^* \exp(\gamma_p). \tag{7}$$

The obtained values of $m_p/m^*$ exceeds the classical limit $\sim 10^5$ for $H = 0$ T and 8 T in both temperature regimes. The obtained values are found to be very large, which again suggests the existence of strong polaron–phonon coupling. It means that the hopping polaronic conduction is due to the non-Schnakenberg adiabatic small polaronic hopping process and gives rise to critical nature.

In order to understand criticality in polaronic hopping conduction, the critical scaling analysis has been utilized, defined as

$$\sigma(T) \sim 1 - \left[T \Big/ \left(\frac{\theta_{\mathrm{D}}}{2}\right)\right]^{-\nu}, \tag{8}$$

where $\nu$ is considered the critical exponent [22]. In Figs. 6 and 7 the logarithmic plots of critical behaviour for $T < T_R = \theta_D/2$ and $T > T_R = \theta_{\mathrm{D}}/2$, respectively, at $H = 0$ T and 8 T are shown. The linear fits to these data points yield values of the critical exponent equal to $\nu = 0.961$ for $H = 0$ T and $\nu = 0.883$ for $H = 8$ T in the temperature regime $T < T_R = \theta_{\mathrm{D}}/2$ and similarly equal to $\nu = 1.115$ for $H = 0$ T and $\nu = 1.074$ for $H = 8$ T in the temperature regime $T > T_R = \theta_{\mathrm{D}}/2$. It can be observed from the obtained values of $\nu$ decreases with the application of the magnetic field and increases with the increase in temperatures above $T_R = \theta_{\mathrm{D}}/2$. This clearly establishes that the activation energies are consistent with polaronic hopping processes and the hopping of charge carriers over the energy barriers is the only essential type of conduction mechanism when charge carriers are thermally activated.

Further, Mott [23] suggested that in the dominant process the activation energy decreases due to the interaction between polarons and lattice phonons. And according to Mott and Davis [24], the hopping of charge carriers occurs beyond the nearest neighbouring available sites at significantly low temperatures $T < T_R = \theta_{\mathrm{D}}/2$ using a process called Mott's-variable range hopping (MVRH) mechanism. The MVRH mechanism has been described mathematically by an Arrhenius-type equation and is given by

$$\sigma = \sigma_0 \exp\left(\frac{-B}{\sqrt[4]{T}}\right), \tag{9}$$

where

$$B = 4\sqrt[4]{\frac{2\alpha^3}{9\pi k_{\mathrm{B}} N(E_{\mathrm{F_M}})}},$$

$$\sigma_0 = \sqrt{\frac{e^2}{2\sqrt{8\pi}}\, \nu_0\, \frac{N(E_{\mathrm{F_M}})}{\alpha\, k_{\mathrm{B}} T}}. \tag{10}$$

In (10), $N(E_{\mathrm{F_M}})$ is referred to as the density of states (DOS) of charge carriers at the Fermi level. In Fig. 8, plots of $\ln(\sigma)$ vs $\sqrt[4]{1/T}$ with linear fit show the experimental data for both $H = 0$ T and 8 T in the temperature regime $T < T_R = \theta_D/2$; fit yields a slope '$B$'. Using the value of $1/\alpha = 10$ Å for the localized states and the slope ($B$) obtained from linear fitting of the conductivity data, the values of $N(E_{\mathrm{F_M}})$ are found and are listed in Table I for both $H = 0$ T and 8 T. It can be observed that the values of $N(E_{\mathrm{F_M}})$ increase with the applied magnetic field, which infers that DOS between the available variable sites also increases [24, 25]. Further, it can be

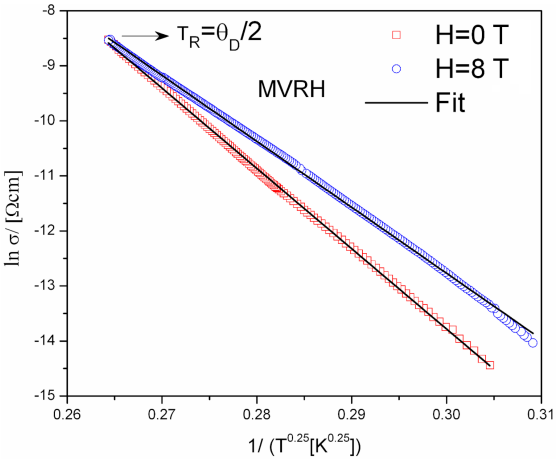


Fig. 8. The plot of $\ln(\sigma/[\Omega\ \mathrm{cm}])$ vs $1/T^{0.25}$ $[\mathrm{K}^{-0.25}]$ for the studied sample at the magnetic field $H = 0$ T and 8 T are shown for $T < T_R$. The solid line is the MVRH model fit.

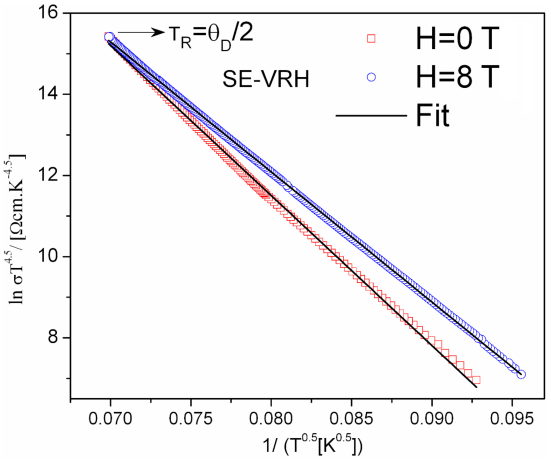


Fig. 9. The plot of $\ln(\sigma T^{4.5}/[\Omega\ \mathrm{cm\ K}^{-4.5}])$ vs $1/T^{0.5}$ $[\mathrm{K}^{-0.5}]$ for the studied sample at the magnetic field $H = 0$ T and 8 T are shown for $T < T_R = \theta_\mathrm{D}/2$. The solid line is the SE-VRH model fit.

clearly observed that the MVRH model fits the experimental data perfectly for $H = 0$ T, but deviates at low temperatures for $H = 8$ T.

This can be understood because at significant low temperatures, the thermal activation becomes insufficient for the polarons and gets altered in the nearest neighbouring sites due to the variation in DOS under the application of magnetic field $H = 8$ T, which does not follow MVRH mechanism. Hence, in order to understand the hopping phenomena under the influence of magnetic field, the Shklovskii–Efros variable range hopping (SE-VRH) mechanism is used. The SE-VRH model can be described as

$$\sigma = \sigma_0 T^{-l} \exp\left(\frac{-T_0}{T}\right)^q, \tag{11}$$

where

$$\sigma_0 = \left[C\,\xi^{11} T_0^{(7+n)q}\right]^{-1}. \tag{12}$$

The best fit to the $\ln(\sigma T^l/[\Omega\ \mathrm{cm\ K}^{-l}])$ vs $1/T^q$ $[\mathrm{K}^{-q}]$ data to the SE-VRH model can be obtained by choosing $l = 4.5$ and $q = 0.5$, as shown in Fig. 9.

Here also it can be observed that for the conductivity data measured at $H = 0$ T the linear fit does not converge fully for the SE-VRH model, whereas for the conductivity data measured at $H = 8$ T the SE-VRH model fits perfectly throughout the whole temperature range of $T < T_R = \theta_D/2$. The SE-VRH model becomes valid when the activation energy is smaller than the coulomb gap ($\Gamma_{CG}$) described as

$$\Gamma_{CG} = k_\mathrm{B}\,(T_0 T_V)^{0.5}, \tag{13}$$

where $T_V$ is the onset of the VRH temperature. The values of $\Gamma_{CG}$ is found to be 17.37 meV for the conductivity data measured at $H = 0$ T and 16.18 meV for $H = 8$ T, respectively. Even though there is not much significant difference in the values of $\Gamma_{CG}$ both for $H = 0$ T and $H = 8$ T, based on the goodness of fit, the hopping conduction is due to the SE-VRH mechanism for $H = 8$ T. Further, the DC electrical conductivity above $T > T_R = \theta_D/2$ neither the MVRH nor SE-VRH model fully fit the data points (figures not shown here), which ruled out the contributions of these two models above $T > T_R = \theta_\mathrm{D}/2$.

Hence the suitable model proposed by Greaves [26] was used to analyse the hopping conduction in this temperature regime ($T > T_R = \theta_\mathrm{D}/2$). The theoretical expression proposed by Greaves is given as

$$\sigma\, T^{0.5} = \sigma_0 \exp\left(\frac{-D}{T^{0.25}}\right), \tag{14}$$

where $D$ is a constant and can be expressed as

$$D = 2.1\left[\frac{\alpha^3}{k_\mathrm{B}\,N(E_{\mathrm{F_G}})}\right]^{0.25}. \tag{15}$$

In Fig. 10 the plots of $\ln(\sigma T^{0.5})$ vs $T^{-0.25}$ with linear fitting the experimental data have been shown for both $H = 0$ T and 8T in the temperature regime $T > T_R = \theta_\mathrm{D}/2$ which yields the value of the slope $D$. From the goodness of the fitting the conductivity data the value of $N(E_{\mathrm{F_G}})$ is calculated and listed in Table I.

From Table I it can be observed that the values of $N(E_{\mathrm{F_M}})$ and $N(E_{\mathrm{F_G}})$ obtained from Mott's variable range hopping (MVRH) and Greave's variable range hopping (GVRH), respectively, are found to be comparable, even though they tend to operate in two different temperature regimes $T < T_R = \theta_\mathrm{D}/2$ and $T > T_R = \theta_\mathrm{D}/2$, respectively. This may be due to the thermal agitation occurring between the phonon-assisted polaronic hopping, which collide frequently while finding the nearest neighbouring sites. In order to understand the effect of thermal

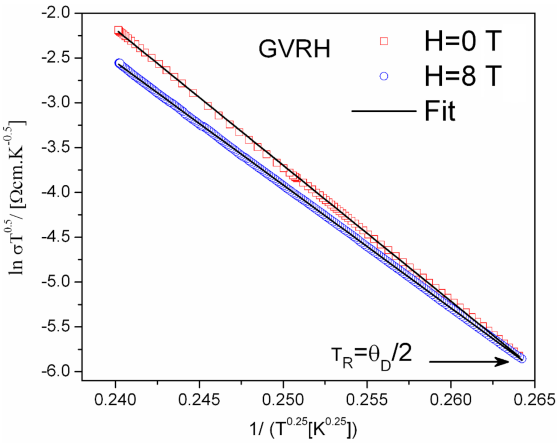


Fig. 10. The plot of $\ln(\sigma T^{0.5}/[\Omega \text{ cm } \mathrm{K}^{-0.5}])$ vs $1/T^{0.25}$ $[\mathrm{K}^{-0.25}]$ for the studied sample at the magnetic field $H = 0$ T and 8 T are shown for $T > T_R = \theta_D/2$. The solid line is the model fit.

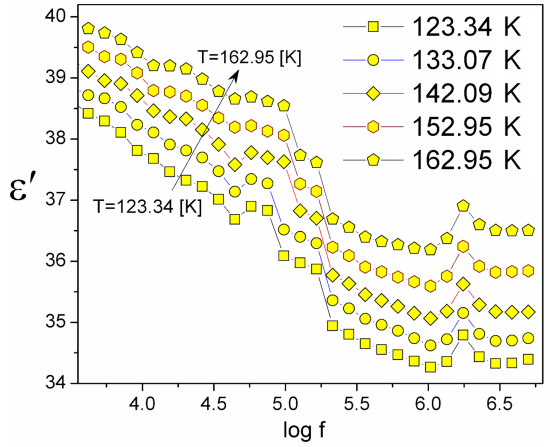


Fig. 11. Temperature-dependent real part of dielectric permittivity, $\varepsilon'$, as a function of frequencies are displayed for various temperatures.

agitation influencing the nearest neighbouring sites the mean hopping distance $R_h$ and the hopping energy $E_h$ required for conduction is calculated using the relations given by

$$R_h = \frac{3}{8}\alpha \left(\frac{B}{T}\right)^{0.5} \tag{16}$$

and

$$E_h = \frac{1}{4} k_B T^{3/4} B^{1/5}, \tag{17}$$

for both $H = 0$ T and 8 T. The obtained values of $R_h$ and $E_h$ are shown in Table I. They are almost comparable for both $H = 0$ T and $H = 8$ T, which indicates the negligible effect of the applied magnetic field since high temperature random fluctuations are predominant.

In Fig. 11, the temperature-dependent real part of dielectric permittivity, $\varepsilon'$, as a function of frequencies measured for various temperatures is

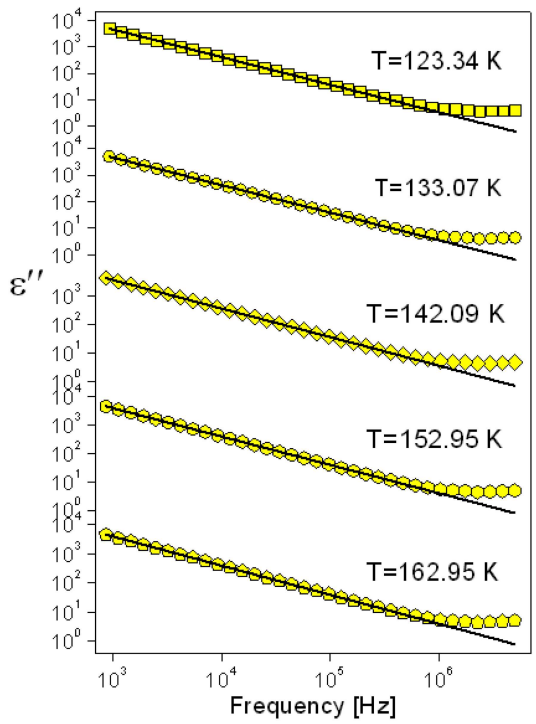


Fig. 12. Frequency dependent dielectric permittivity $\varepsilon''$ at various temperatures. Solid lines are the experimental fit.

shown. It can be observed that the $\varepsilon'$ values increase with increasing temperatures and decreases with increasing frequencies. The high value of the dielectric permittivity $\varepsilon'$ in the low frequency region is due to the overwhelming dominance of the electrode polarization region when it is subjected to the time dependent electric field. Upon increase in the frequency, the decrease in the values of $\varepsilon'$ can be attributed to the various dielectric relaxation processes, which creates a complex region for the dipoles to align under the application of the electric field. The higher value of $\varepsilon'$ at low frequencies is due to the enhancement of the polaronic conductivity and follows the theoretical relation given as $\sigma_k = \sum_k (q_k n_k \mu_k)$. Also, the imaginary part of the dielectric permittivity, $\varepsilon''$, plotted against frequencies is shown in Fig. 12 at variable temperatures. It can be clearly observed that value of $\varepsilon''$ decreases with increasing frequencies, which can be attributed due to the different relaxation mechanisms occurring in the sample.

In order to get the clear understanding of the role of different mechanisms, we analysed the $\varepsilon''$ data with the combined Debye + Maxwell–Wagner (DMW) relaxation mechanisms, which is given by [26]

$$\varepsilon'' = \frac{\left(\frac{f}{f_0}\right)(\varepsilon_S - \varepsilon_\infty)}{1 + \left(\frac{f}{f_0}\right)^2} + \frac{\sigma}{2\pi\epsilon_0 f}, \tag{18}$$

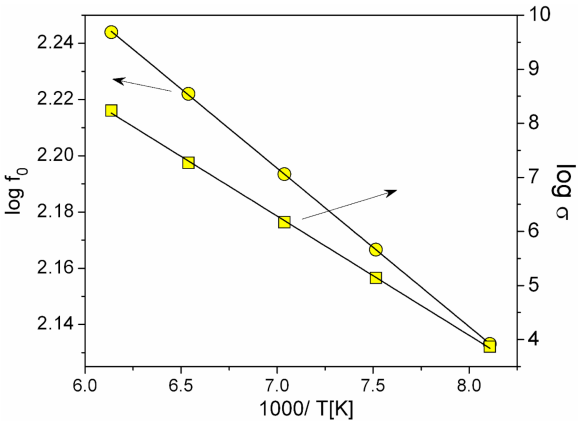


Fig. 13. The plots of $\log(f_0)$ and $\log(\sigma)$ vs $1000/T$ [$K^{-1}$]. Solid lines are linear fitting to the Arrhenius-type plots.

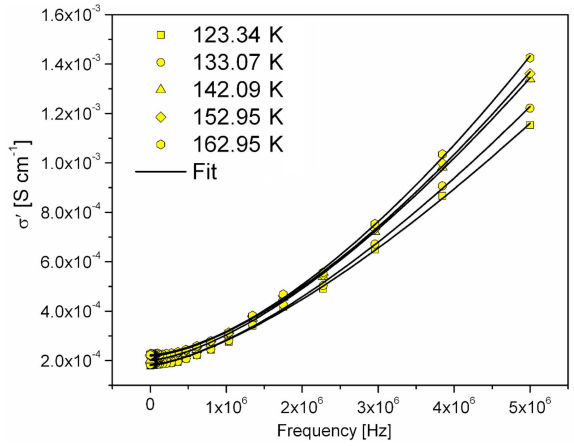


Fig. 14. Frequency dependent real part of the AC conductivity ($\sigma'$) at variable temperatures for the studied sample are shown. Solid lines are the experimental fittings.

where $f_0$ is the relaxation frequency, $\epsilon_0$ is the permittivity in the free space, $\varepsilon_S$ is the static permittivity, $\varepsilon_\infty$ is the relative permittivity at infinite frequency, and $\sigma$ is the conductivity of the sample and depends on Maxwel + Wagner contributions [27].

It can be observed that the experimental data satisfies the combined relation for different high temperatures at lower and intermediate frequencies, but fails at higher frequencies, indicating the absence of space charge polarization. The best fit parameters of $f_0$ and $\sigma$, obtained by fits to the experimental data of $\varepsilon''$, can theoretically be considered to be in accordance with the Arrhenius law [28]. Linear fitting to the plot of $\log(\sigma)$ and $\log(f_0)$ vs $1000/T$ (shown in Fig. 13) yields the activation energy ($E_A$) and relaxation time ($\tau$). The obtained values are found to be $E_A = 0.135$ eV and $\tau = 3.55 \times 10^{-6}$ s, which correlates with the values of $E_A$ obtained from the DC electrical conductivity data for $T < T_R$.

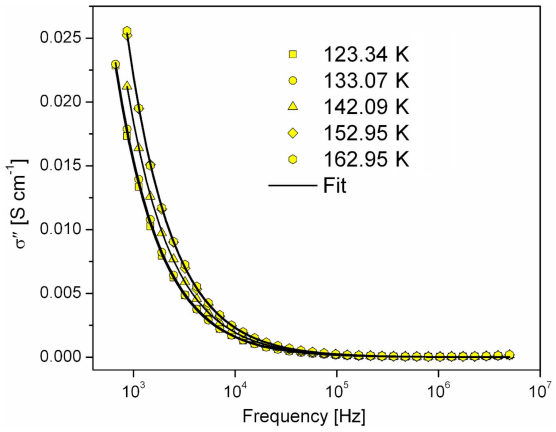


Fig. 15. Frequency dependent imaginary part of the AC conductivity ($\sigma''$) at variable temperatures for the studied sample are shown. Solid lines are the experimental fittings.

Further, the AC conductivity ($\sigma_{AC}$) vs frequency at variable temperatures was studied to understand the complex transport phenomena and establish a suitable correlation with the DC conductivity. Conductivity measurements are considered to be the most prominent representation in order to correlate macroscopic analysis of microscopic transport properties [29]. The AC conductivity has been computed from the real and imaginary parts of the impedance data measured at various temperatures. The total complex conductivity $\sigma^*(\omega)$ is expressed as $\sigma^*(\omega) = \sigma'(\omega) + i\sigma''(\omega)$. As shown in Fig. 14, $\sigma'(\omega)$ exhibits two distinct features, i.e., one at low frequencies where the increase in $\sigma'(\omega)$ is associated with the electrode polarization region and the other at high frequencies the polaron possess short-range path. For any given specific frequency, the transition from the long-range to short-range path can be termed as the hopping frequency and a successful hopping occurs when the polaron hops to a new site [29].

The high-frequency Jonscher power law is also incorporated to the mentioned equations of the real and imaginary part of the AC conductivity. This results in

$$\sigma'(\omega) = \sigma_p \left[1 + \left(\frac{\omega}{\omega_q}\right)^n\right] \tag{19}$$

and

$$\sigma''(\omega) = B\omega^m, \tag{20}$$

where the exponents $n$ and $m$ have the values less than unity [30]. Equations (19)–(20) are used to fit $\sigma'(\omega)$ and $\sigma''(\omega)$ under constant temperatures, as shown in Figs. 14 and 15, respectively. The exponents $n$ and $m$ ranging from 0.897 to 0.989 was obtained satisfying the Jonscher power law dependency condition. In order to understand the correlation between DC conductivity, the temperature dependent real part of the AC conductivity data

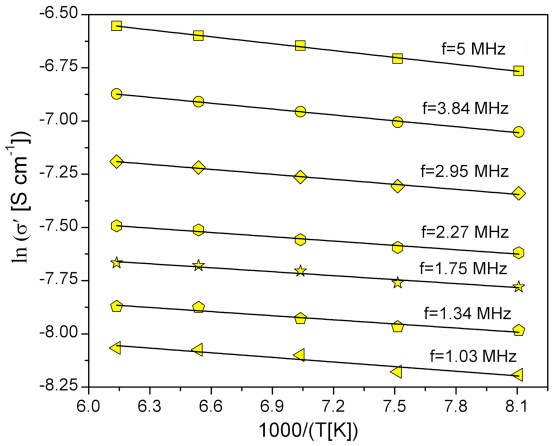


Fig. 16. The plot of $\ln(\sigma\prime)$ vs $1000/T$ [$K^{-1}$] plots for different frequencies are shown. Solid lines are model fit.

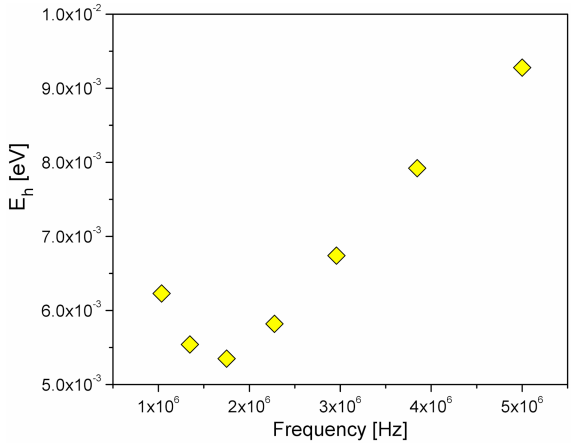


Fig. 17. Variations of the activation energies with respect to the measured frequencies are shown.

was extracted for different frequencies in the range of 1–5 MHz and analysed using the TAC model as explained earlier [16]. The linear fits to the plot $\ln(\sigma')$ vs $1000/T$ [$K^{-1}$] shown in Fig. 16 yield the thermally activated hopping energies ($E_h$). The obtained values of $E_h$, which are few meV for low frequencies (see Fig. 17), are agreeable with the theoretically calculated values of $E_h$ listed in Table I for DC conductivity. Hence, correlations between DC and AC conductivity in the studied sample is possible.

## 4. Conclusions

In the present work the electrical transport and dielectric properties of the sample is studied in detail. The sample exhibits insulating (semiconducting) nature throughout the measured temperature range without any phase transition. This nature is common observed in the samples containing $Bi^{3+}$ as dopant at La site in the original sample of $LaMnO_3$ group, which hampers the local ordering due to the existence of isolated $6s^2$ lone pair of electrons which disrupts the oxygen octahedra structure. Even low concentration of $Bi^{3+}$ also produces enough hybridization of the $2p$ orbitals of octahedra, which in turn induces frustrations. The low-temperature DC electrical conduction is due to the MVRH polaronic hopping mechanism in the absence of the magnetic field ($H = 0$ T). But under the presence of magnetic field ($H = 8$ T) the DC electrical conduction switches to the SE-VRH polaronic hopping mechanism due to various competing localized structures. The high-temperature DC electrical conduction is governed by the GVRH polaronic hopping mechanism both at $H = 0$ T and 8T. The variation in the values of dielectric permittivity with the increase in the frequencies can be attributed to the different relaxation mechanisms, in particular the combined effect of DMW type. Furthermore, the AC conductivity studies correlate with the DC electrical conductivity measurements via activated polaronic hopping mechanism.

## Acknowledgments

The theoretical aspect of this research was supported in part by the International Centre for Theoretical Sciences (ICTS) for participating in the program — Condensed Matter meets Quantum Information (code: ICTS/COMQUI2023/09) and Engineered 2D quantum materials, 2024. The author (V.P.K) is greatly indebted to DAE-BRNS for junior research fellowship (JRF) and senior research fellowship (SRF) (2011–2015), Maharaja Research Foundation (MRF) for the extended SRF (2015–2017) during the Ph.D. tenure at Maharaja Institute of Technology (MIT), Mysore. V.P.K. is very thankful to the Indian Institute of Science, Bangalore, for project research fellowship (2017–2018). V.P.K. is immensely grateful to Dr. Rajeev Rawat and Mr. Sachin Kumar of UGC-DAE CSR, Indore, for electrical conductivity measurements. V.P.K. gratefully acknowledges Dr. S.K. Deshpande of UGC-DAE CSR, Mumbai, for dielectric measurements. Also, V.P.K. thanks Dr. Ravi L. Hadimani, Virginia Commonwealth University, USA, and Dr. David C. Jiles, Anson Marston Distinguished Professor of Engineering and Palmer Endowed Department Chair in Electrical & Computer Engineering, Iowa State University, USA, for continuous support, motivation and inspirations.

## References

[1] J.L. Garcia-Munoz, C. Frontera, M.A.G. Aranda, A. Llobet, C. Ritter, *Phys. Rev. B* **63**, 064415 (2001).

[2] S. Hanif, M. Hassan, S. Riaz, S. Atiq, S.S. Hussain, S. Naseem, G. Murtaza, *Results Phys.* **7**, 3190 (2017).

[3] V. Punith Kumar, *Bull. Mater. Sci.* **44**, 136 (2021).

[4] J.X. Flores-Lasluisa, F. Huerta, D. Cazorla-Amorós, E. Morallón, *Energy* **247**, 123456 (2022).

[5] Y.D. Zhao, J. Park, R.-J. Jung, H.-J. Noh, S.-J. Oh, *J. Magn. Magn. Mater.* **280**, 404 (2004).

[6] Y. Ishii, A. Ikeda, M. Tokunaga, K. Kindo, A. Matsuo, Y.H. Matsuda, *J. Phys. Soc. Jpn.* **92**, 074702 (2023).

[7] P. Wadhwa, T.J.D. Kumar, A. Shukla, R. Kumar, *Solid State Commun.* **358**, 114976 (2022).

[8] T. Izgi, V.S. Kolat, N. Bayri, H. Gencer, S. Atalay, *J. Magn. Magn. Mater.* **372**, 112 (2014).

[9] I.O. Troyanchuk, D.V. Karpinsky, M.V. Bushinsky, V.A. Khomchenko, G.N. Kakazei, J.P. Araujo, M. Tovar, V. Sikolenko, V. Efimov, A.L. Kholkin, *Phys. Rev. B* **83**, 054109 (2011).

[10] T. Ogawa, A. Sandhu, M. Chiba, H. Takeuchi, Y. Koizumi, *J. Magn. Magn. Mater.* **290–291**, 933 (2005).

[11] H. Woo, T.A. Tyson, M. Croft, S.-W. Cheong, J.C. Woicik, *Phys. Rev. B* **63**, 134412 (2001).

[12] V. Punith Kumar V., *Ind. J. Phys.* **96**, 1393 (2022).

[13] V. Punith Kumar, *J. Low Temp. Phys.* **218**, 451 (2025).

[14] Y. Endoh, K. Hirota, S. Ishihara et al., *Phys. Rev. Lett.* **82**, 4328 (1999).

[15] H. Hirashima, D. Arai, T. Yoshida, *J. Am. Ceram. Soc.* **68**, 486 (1985).

[16] L. Murawski, C.H. Chung, J.D. Mackenzie, *J. Non-Cryst. Solids* **32**, 91 (1979).

[17] T.G. Castner, in: *Hopping Transport in Solids*, Eds. M. Pollak, B. Shklovskii, Elsevier, Amsterdam 1991, Ch. 1, p. 1.

[18] J. Schnakenberg, *Phys. Status Solidi*, 28, 623 (1968).

[19] N.F. Mott, E.A. Davis, *Electronic Processes in Non-Crystalline Materials*, 2nd ed., Oxford University Press, 1971.

[20] T. Holstein *Ann. Phys.* **8**, 343 (1959).

[21] S. Chakraborty, M. Sadhukhan, D.K. Modak, B.K. Chaudhuri, *J. Mater. Sci.* **30**, 5139 (1995).

[22] R. Laiho, K.G. Lisunov, E. Lähderanta, V.S. Stamov, V.S. Zakhvalinskii, P. Colomban, P.A. Petrenko Y.P. Stepanov, *J. Phys. Condens. Matter* **17**, 105 (2005).

[23] N.F. Mott, *J. Non-Cryst. Solids* **1**, 1 (1968).

[24] N.F. Mott, E.A. Davis, K. Weiser, *Phys. Today* **25**, 55 (1972).

[25] H. Sakata, K. Sega, B.K. Chaudhuri, *Phys. Rev. B Condens. Matter* **60**, 3230 (1999).

[26] G.N. Greaves, *J. Non-Cryst. Solids* **11**, 427 (1973).

[27] K.C. Khao, *Dielectric Phenomena in Solids*, Elsevier, 2004.

[28] B.I. Shklovskii, A.L. Efros, *Electronic Properties of Doped Semiconductors*, Springer, Berlin 1984.

[29] Y.J. Wong, J. Hassan, M. Hashim, *J. Alloys Compd.* **571**, 138 (2013).

[30] A. Arya, A.L. Sharma, *J. Mater. Sci. Mater. Electron.* **29**, 17903 (2018).